Torque Ripple Compensation for IPMSM with Minimum Loss

Torque Ripple Compensation for IPMSM with Minimum Loss

Vasyl Varvolik[1,4], Paolo Pescetto[2], Simone Ferrari[2], Shuo Wang[1]
Michele Degano[3], Giampaolo Buticchi[1], Gianmario Pellegrino[2]
[1]*Key Laboratory of More Electric Aircraft Technology of Zhejiang Province*
University of Nottingham Ningbo China, Ningbo, China
[2] *Dipartimento Energia Galileo Ferraris*, *Politecnico di Torino*, Turin, Italy
[3] *Power Electronics, Machines and Control Group*,*University of Nottingham*, Nottingham, UK
[4] *Institute of Electrical Drives and Power Electronics*, *Johannes Kepler University*, Linz, Austria
Emails: varvolik@ieee.org, paolo.pescetto@polito.it

***Abstract*—This study presents an in-depth analysis of the torque ripple compensation methods, comparing current harmonics injection (CHI) in d-axis, q-axis, and dq-axes including instant Maximum Torque Per Ampere and Direct Flux-and-Torque Control, which targets the minimum loss for an interior Permanent Magnet synchronous motor. The performance of different CHIs has been evaluated by finite element simulations, highlighting the importance of the selection of the CHI technique for torque ripple compensation considering minimum total loss.**

***Index Terms*—minimum loss, spatial harmonics, synchronous motor drive, torque ripple.**

I. Introduction

In order to break transport dependency on oil and decrease greenhouse-gasses emissions, modern transportation is moving at a breathtaking pace towards full electrification. Permanent Magnet (PM) synchronous motor drives have been experiencing a booming advancement as one of the key technologies enabling proactive penetration of electric vehicles (EVs) thanks to their high torque density and efficiency [1]. Among PM motor topologies, an interior Permanent Magnet synchronous motor (IPMSM) is the most promising candidate for traction applications since its anisotropic rotor structure is able to provide the reluctance torque in addition to the PM flux torque [2]. On the other hand, the interaction between the rotor anisotropy and the stator magneto-motive force (MMF) yields torque ripple, leading to acoustic noise and vibration, which is intolerable in traction applications [3].

Over the last two decades, extensive research has been done to address torque ripple reduction by means of motor design optimization or active motor control [4], [5]. Several optimization techniques have been presented in the literature in order to achieve torque ripple reduction through optimal machine design employing rotor and stator skewing [3], asymmetric rotor topologies [6], PMs pole shaping [7]. However, torque ripple can be reduced to a certain extent while increasing the manufacturing complexity and optimization time.

The active motor control techniques are based on the injection of current harmonics cancelling out the corresponding torque ripple harmonics [8]. The existing techniques for torque ripple reduction of PMSMs can be further split into feedback-based and torque model-based methods. In the former group, the torque ripple is directly measured using a torque sensor [9] or indirectly derived by means of speed [10]–[12] and vibration measurements [13]. Even though feedback-based methods can deliver good performance, the inertia of the system can significantly attenuate the speed harmonics, particularly at high-speed regions, thus deteriorating the harmonics extraction [14], while direct torque measurement is hindered due to the high cost and limited bandwidth of the sensor.

An important prerequisite for torque ripple reduction by torque model-based methods is setting up an accurate torque model in order to derive the current reference trajectories. The torque model should be established including the main torque ripple components due to spatial harmonics of flux linkages owing to PMs, stator currents, rotor saliency, and cogging torque [15]. Therefore, it is possible to determine the optimal current trajectory that corresponds to the minimum torque ripple. It should be noted that the flux linkage harmonics due to stator currents vary with load due to the presence of magnetic saturation [10], resulting in a more complex mechanism of the torque ripple generation in the case of IPMSM compared to surface-mounted PMSM(SPMSM) [16].

After setting up the torque model, an infinite number of current trajectories for one torque setpoint can be derived theoretically. For this reason, the optimization algorithms with certain constraints are commonly applied, including Lagrange multiplier [17], [18], genetic algorithm [19], self-learning [20], fuzzy logic [21], particle swarm optimization (PSO) [22]. The typical constraint is minimizing the copper loss due to the CHI, while the iron loss is disregarded. The instant maximum torque per ampere (IMTPA) control concept proposed in [23], based on the actual torque maps allows computation of the dq-current trajectories according to the torque reference which guarantees the minimum copper loss. The studies in [24] and [25] propose the integration of iron loss resistance and the IPMSM model using multiple reference theory (MRF). As a result, the reference currents can be obtained, minimizing both copper and iron losses. The LUT-based iron loss model for SPMSM [26] can provide higher accuracy compared to the resistance model for current trajectories optimization. However, the conventional iron loss models consider only iron loss due to the fundamental harmonic of the magnetic flux density [27], neglecting magnetic saturation and high-order harmonics. Furthermore, the flux density distortions due to the CHI for torque ripple reduction generate extra iron loss should be considered. Consequently, the FE analysis can be employed as an accurate analytical estimation of the iron loss in the case of multiple flux density harmonics is not trivial.

In this paper, an in-depth analysis is carried out to determine the CHI technique for torque ripple compensation with minimum loss. Separate d-axis and q-axis CHIs along with two types of dq-axes CHIs, namely IMTPA [23] and Direct Flux-and-Torque Vector Control (DTFC) [5] are compared.

II. Torque ripple analysis

A. Considered motor

Fig. 1 shows a sketch of the IPMSM prototype used as a study case, and the main data is summarized in the Appendix.

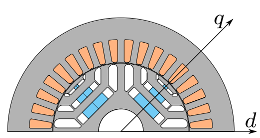

Fig. 1. Cross-section of the IPMSM.

B. Torque ripple of IPMSM

Torque ripple is produced by the interaction of the spatial harmonics of the stator MMF and the rotor saliency [28]. The torque can be derived from the power balance of the electromechanical energy conversion in a rotating reference frame assuming constant d-axis and q-axis currents as [29]

$$\begin{aligned} T_m =& \frac{3}{2} p_n \left(\psi_d i_q - \psi_q i_d \right) + \frac{3}{2} \left(i_d \frac{\partial \psi_d}{\partial \theta_m} + i_q \frac{\partial \psi_q}{\partial \theta_m} \right) - \frac{\partial W_m}{\partial \theta_m} \\ =& \frac{3}{2} p_n (\psi_d i_q - \psi_q i_d) + \frac{\partial W_{m.c}}{\partial \theta_m} = T_{m.e1} + T_{m.e2} \qquad (1) \end{aligned}$$

where i_d, i_q are the stator current components, ψ_d, ψ_q are the flux linkage components of (d-q) axes, θ_e is the electrical position, p_n is the pole pairs number, and $W_{m.c}$ is the magnetic coenergy.

It should be noted that the magnetic energy-flux linkages relationship can be used to set up the accurate torque model using experimental identification methods [30], [31].

Fig. 2 shows the torque waveforms and FFT spectra of considered IPMSM under different load conditions along the MTPA trajectory ($0.5T_n$, T_n, and $2T_n$).

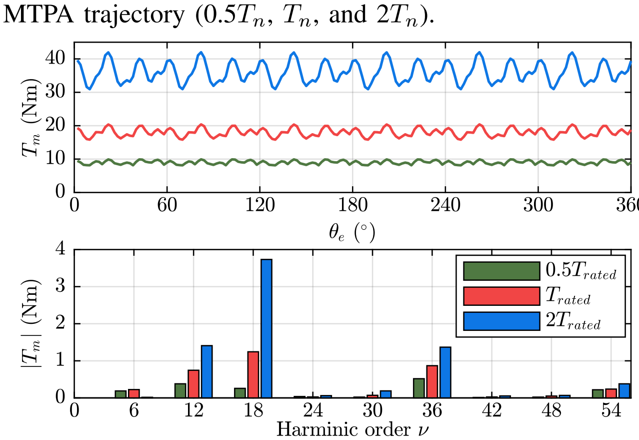

Fig. 2. Torque waveforms with respect to the rotor position and FFT spectra.

Analyzing torque waveforms and FFT spectra, only harmonics multiple of 6 are considered owing to the distributed winding configuration. The dominant torque ripple harmonics correspond to the slotting subharmonics of orders 12, 18, and 36, with amplitudes significantly increasing with the load. It is worth noting that the main contribution to the the torque ripple is due to the coenergy variation $T_{m.e2}$ linked to the rate of change of flux linkage harmonics, while $T_{m.e1}$ is commonly referred to as the average torque. In case of no-load condition, $T_{m.e2}$ is identical to the cogging torque [23].

In order to underline the effect of saturation, the torque maps of different harmonics are presented in Fig. 3.

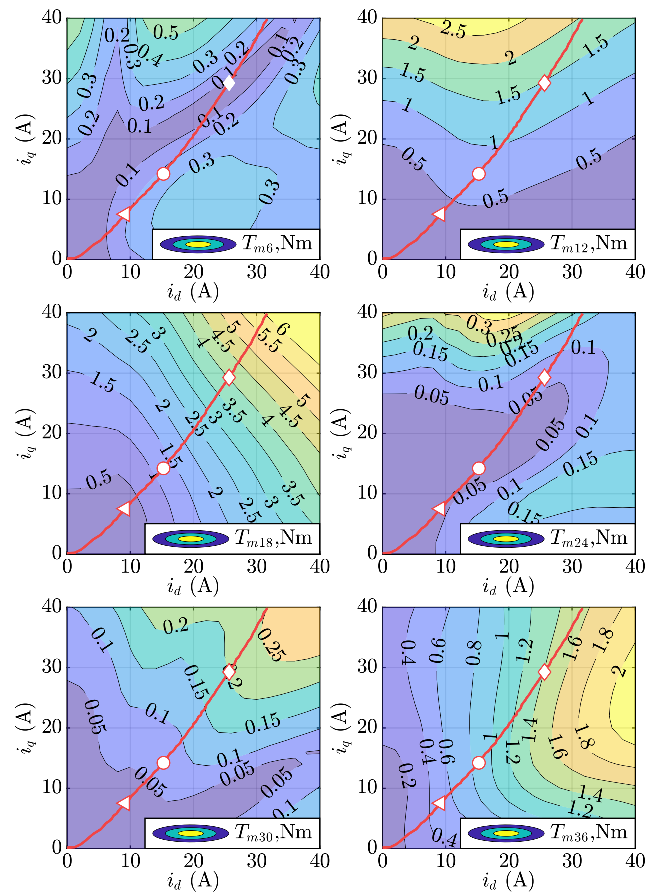

Fig. 3. Torque ripple harmonics amplitude maps (MTPA trajectory is in red with selected operating points - $0.5T_n(\triangleleft)$, $T_n(\circ)$, and $2T_n(\diamond)$).

The presented maps indicate that the amplitudes of torque ripple harmonics are highly nonlinear and mainly increase with magnetizing current, whereas higher saturation occurs. It can be noted that the highest amplitudes of torque ripple harmonics correspond to the slotting subharmonics.

III. Current trajectories for torque ripple compensation

The MTPA strategy is commonly used to deliver high-efficiency control of the drive system by obtaining the maximum torque for a given current amplitude, thus minimizing the copper loss. However, the presence of high-order harmonics injected for torque ripple compensation inevitably incurs extra copper and iron losses [8]. The torque ripple can generally be compensated by utilizing the d-axis, q-axis, or combined dq-axes current injections while incurring different loss levels. Therefore, the comparative analysis of different CHIs is carried out to determine the CHI technique for torque ripple compensation with minimum loss.

A. d-axis and q-axis CHIs

In order to derive the current injection trajectories employing the d-axis and q-axis, the torque model is linearised around a specified working point (i_{d0}, i_{q0}) defined by the constant torque reference command T_m^* according to the fundamental MTPA trajectory. For linearisation, the current components are represented as follows

$$i_d = i_{d0} + \delta i_d\,, \qquad i_q = i_{q0} + \delta i_q \tag{2}$$

where δi_d and δi_q are small current variations with respect to the fundamental values for torque ripple reduction.

The torque variation around the reference T_m^* is represented by applying the first-order Taylor series approximation as

$$\delta\tau_m = \tau_{md}\delta i_d + \tau_{mq}\delta i_q \tag{3}$$

where $\delta\tau_m = T_m^* - T_m(i_{d0}, i_{q0})$, τ_{md} and τ_{mq} is incremental torque with respect to the d-axis and q-axis currents, respectively, defined as:

$$\tau_{md} = \frac{\partial T_m(i_d, i_q)}{\partial i_d}\bigg|_{i_d=i_{d0}, i_q=i_{q0}} \tag{4}$$

$$\tau_{mq} = \frac{\partial T_m(i_d, i_q)}{\partial i_q}\bigg|_{i_d=i_{d0}, i_q=i_{q0}} \tag{5}$$

By setting $\delta\tau_m = 0$, the torque ripple can be compensated by calculating δi_d and δi_q for every rotor position (Fig. 4) as

$$\begin{aligned} &\delta i_d = \delta\tau_m/\tau_{md}, \delta i_q = 0, \quad && d\text{-axis injection} \\ &\delta i_d = 0, \delta i_q = \delta\tau_m/\tau_{mq}, \quad && q\text{-axis injection} \end{aligned} \tag{6}$$

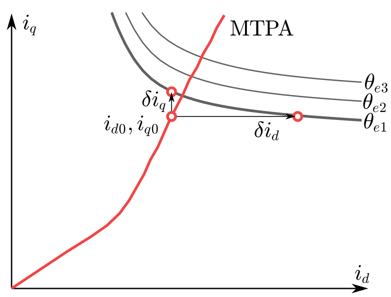

Fig. 4. Isotorque curves at the fixed rotor positions for current trajectory derivation by d-axis and q-axis CHIs.

B. dq-axes CHI: Instant MTPA

Instant MTPA concept is formulated as a nonlinear constrained optimization problem, defined as follows [23]

$$\min(i_d^2 + i_q^2) \quad \text{subject to} \quad \tau_m = T_m^*, \tag{7}$$

In fact, the optimization problem is solved for each rotor position by using an isotorque curve corresponding to the reference torque, allowing to find the minimum current amplitude $|i|$ with respect to the current phase φ along the isotorque curve which yields the minimum copper loss as shown in Fig. 5.

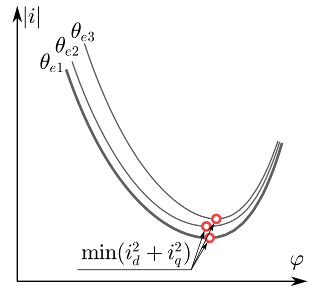

Fig. 5. Isotorque curves at the fixed rotor positions for current trajectory derivation by instant MTPA

C. dq-axes CHI: Direct Flux-and-Torque Vector Control

The DTFC operates in the stator flux reference frame, whereby the flux amplitude ψ and torque can be controlled by means of the d_s-axis voltage being aligned with the stator flux vector and the q_s-axis voltage, respectively [5]. The angle $\hat{\theta}_s$ is the phase of the observed flux linkage with respect to the stator α-axis.

The voltage components u_{ds}, u_{qs} in the stator flux reference frame ($d_s - q_s$) are expressed as

$$\begin{cases} u_{ds} &= R_s i_{ds} + \dfrac{d\psi}{dt} \\ u_{qs} &= R_s i_{qs} + \psi\left(\omega_e + \dfrac{d\delta}{dt}\right) \end{cases} \tag{8}$$

where i_{ds}, i_{qs} are the stator current components, R_s is the stator resistance, ω_e is the electrical speed, δ is the load angle.

The fundamental torque can be expressed as

$$T_{dq} = \frac{3}{2} p_n \psi i_{qs} \tag{9}$$

The flux reference ψ^* is defined by the MTPA, allowing the implementation of field weakening (FW) by saturating ψ_{max} according to the speed and the actual dc-link voltage u_{dc} as

$$\psi_{max} = \frac{\sqrt{\dfrac{u_{dc}^2}{3} - R_s i_{ds}^2} - R_s|i_{qs}|}{|\omega_e|} \approx \frac{\dfrac{u_{dc}}{\sqrt{3}} - R_s|i_{qs}|}{|\omega_e|} \tag{10}$$

The control scheme for the torque ripple compensation using the DTFC is depicted in Fig. 6.

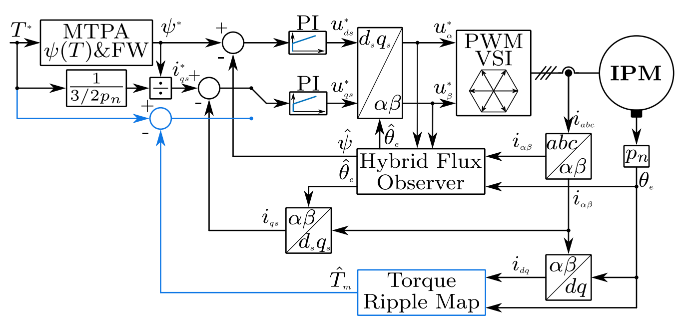

Fig. 6. Block diagram of the DTFC.

Flux amplitude and torque are closed-loop controlled by two dedicated PI current controllers. The Hybrid Flux Observer (HFO) estimates the amplitude and phase of flux linkage, while the $dq\theta$ torque model organized as a 3D look-up table is used to provide torque feedback.

The reference CHI trajectories with corresponding FFT spectra for the rated condition of the considered IPMSM are depicted in Fig. 7. It should be noted that to derive the CHI trajectories, an accurate torque model is required.

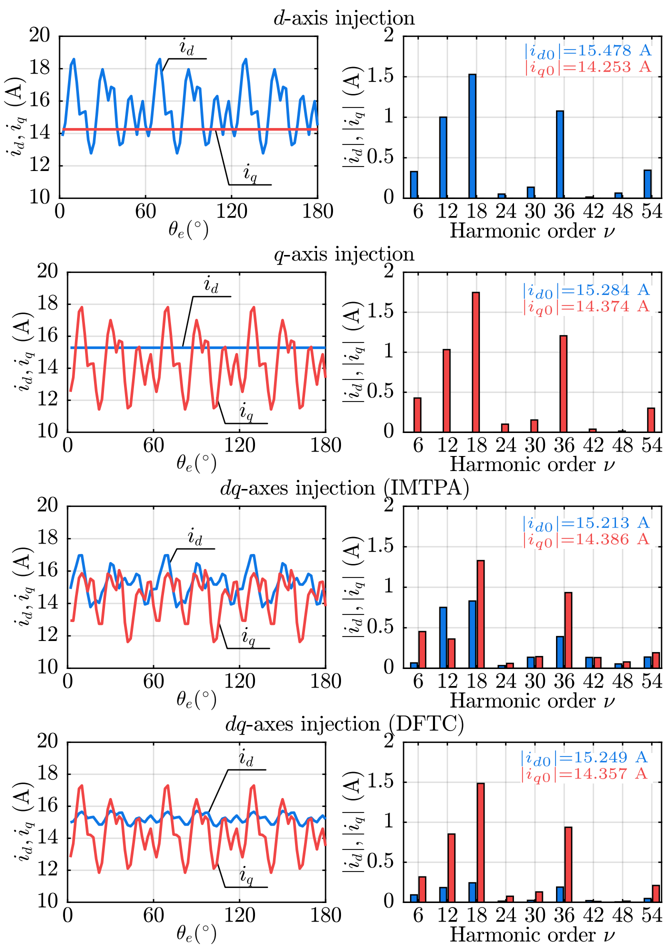

Fig. 7. Current waveforms with FFT spectra for torque ripple compensation by considered CHIs.

D. Losses due to CHIs

As previously mentioned, the high-order current harmonics injection inevitably results in additional copper and iron losses. The induced copper loss is assumed to be proportional to the square of the current harmonic amplitudes as

$$P_{cu}^{h} = \sum_{\nu=6,12..} (i_{d\nu}^2 + i_{q\nu}^2) R_s \tag{11}$$

where $i_{d\nu}$ and $i_{q\nu}$ are amplitudes of high-order current harmonics.

In the case of iron loss, the two-term model can be used for the iron loss estimation assuming a sinusoidal magnetic flux density as [32]

$$P_{fe} = P_{fe.e} + P_{fe.h} = k_e f^2 B_m^2 + k_h f B_m^2 \tag{12}$$

where $P_{fe.e}$, $P_{fe.h}$ are eddy current and hysteresis losses per weight, k_e, k_h are the material loss coefficients, B_m and f are the amplitude and frequency of the flux density.

However, the additional iron loss is incurred due to the presence of flux density harmonics as well as the CHI for torque ripple compensation. Therefore, the FE analysis can be used in order to estimate the flux density waveforms in various parts of the machine. The total iron loss can be calculated by the following expressions with the Fourier transformation as [33], [34]

$$P_{fe.e} = \frac{k_e}{2\pi^2} \text{Mean Square}\left(\frac{dB}{dt}\right) = k_e f^2 \sum_{\nu \geq 1} |\nu B_\nu|^2 \tag{13}$$

$$P_{fe.h} = k_h f B_m^2 \left(1 + \frac{k_{hy}}{B_m} \sum_{i=1}^{n} \Delta B_i\right) \tag{14}$$

where B is the instantaneous flux density, B_ν is the amplitude of ν^{th} flux density harmonic, ΔB_i is the local amplitude of flux density associated with minor loops; n is the number of minor loops, and k_{hy} is a constant in the range of 0.6 to 0.7.

The analysis of (13) and (14) suggests that both eddy current and hysteresis losses tend to increase under non-sinusoidal flux density. Especially considering that the CHI generates minor hysteresis loops leading to significant flux density distortion. The area of the hysteresis minor loops depends on the amplitude of injected current harmonics.

It should be noted that PM iron loss does not have a significant influence as the PWM switching time harmonics are not considered in this work.

IV. Simulation Results

In order to make an accurate comparison of the considered CHI strategies for torque ripple compensation, the FE-based simulations of IPMSM based on 2D FEA FEMM solver are run (Fig. 8). It allows the prediction of flux linkage and torque waveforms, the copper and iron losses under different load conditions and speeds.

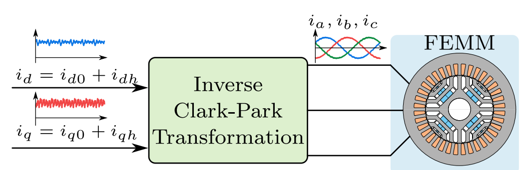

Fig. 8. Block diagram for FE-based simulations.

Fig. 9 shows the waveforms of the flux linkages and the torque under different CHIs corresponding to the reference CHI trajectories in Fig. 7. As can be seen, the torque ripple can be well-compensated by employing the d-axis, q-axis, and dq-axes (IMTPA and DFTC) CHI trajectories, while introducing different levels of flux linkage distortions. Owing to the magnetic anisotropy of IPMSM, the level of flux linkage distortions is expected to depend on the CHI orientation, with the highest distortion occurring due to the d-axis CHI and the lowest due to the q-axis CHI. In fact, the flux linkage amplitude can be directly controlled by the dq-axes CHI based on DFTC allowing to compensate for the torque ripple with the lowest flux linkage distortions.

For the sake of better illustration, the FFT spectra of the flux linkages and torque are shown in Fig. 10.

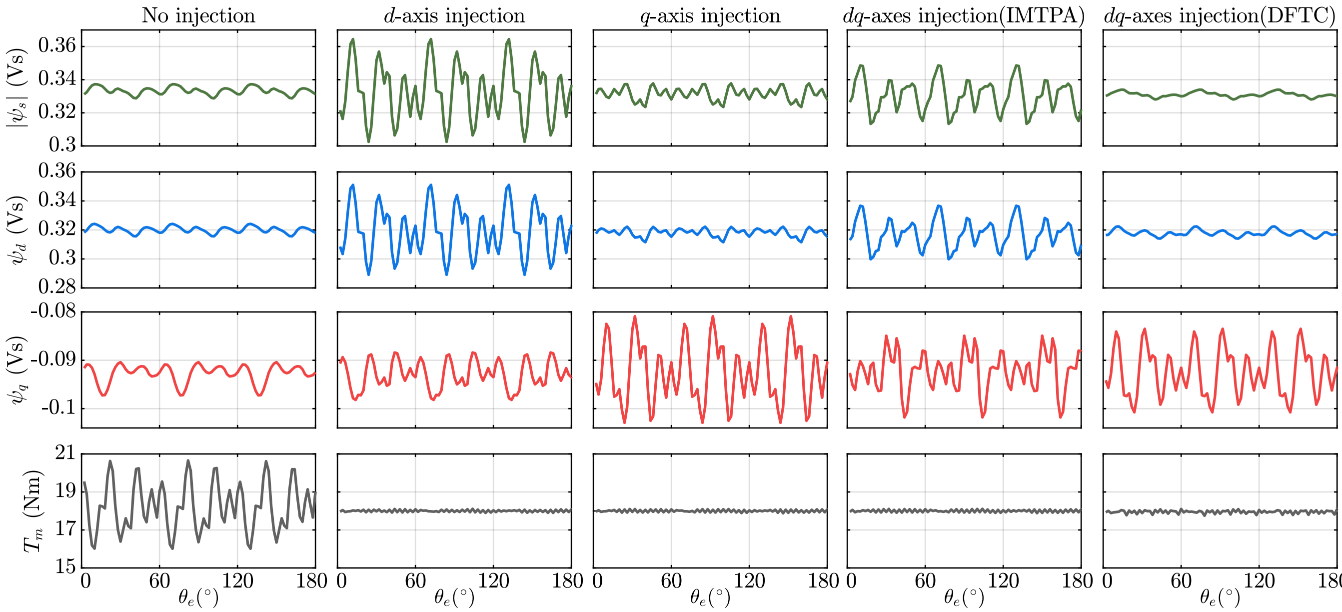

Fig. 9. Comparison of torque ripple compensation for the rated condition by different injection strategies.

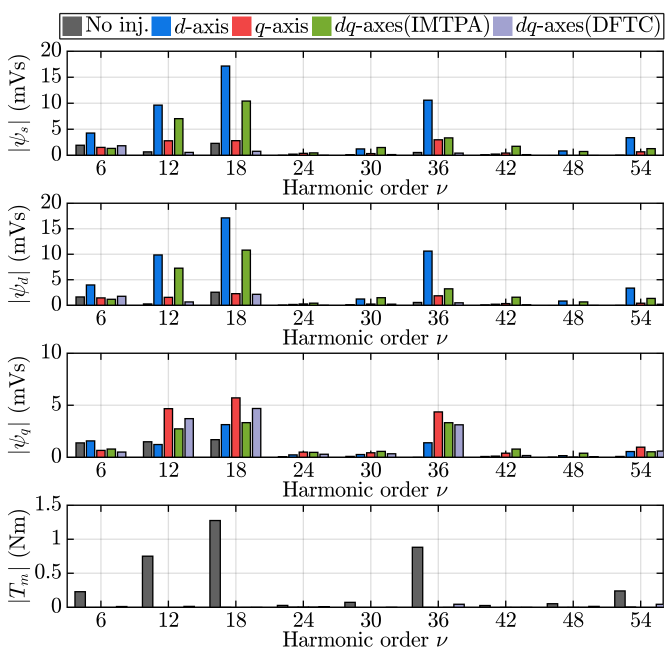

Fig. 10. Comparison of flux linkage and torque FFT spectra.

To highlight the copper loss due to CHIs, the copper loss increments ΔP_{cu} are introduced as the difference of copper loss under the CHI P_{cu}^{CHI} and sinusoidal currents P_{cu}^{sin} as follows

$$\Delta P_{cu} = P_{cu}^{CHI} - P_{cu}^{sin} \tag{15}$$

Fig. 11 shows the comparison of the copper loss increments along the MTPA trajectory. It is expected that the dq-axes (IMTPA) CHI incurs the lowest copper loss. It is worth noting that the fundamental copper loss is inherently minimized for d-axis, q-axis, and dq-axes (DFTC) CHIs as the fundamental current/flux references are retrieved by the MTPA.

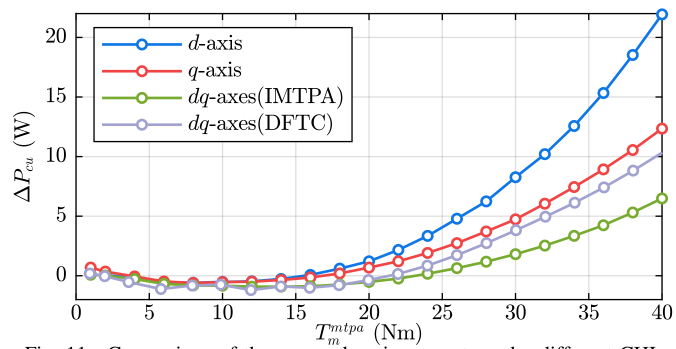

Fig. 11. Comparison of the copper loss increments under different CHIs.

Similarly, the iron loss increments ΔP_{fe} are presented, indicating the iron loss incurred by the CHI for torque ripple compensation as

$$\Delta P_{fe} = P_{fe}^{CHI} - P_{fe}^{sin} \tag{16}$$

Fig. 12 shows the comparison of the iron loss increments along the MTPA trajectory estimated by means of the 2D FEA solver. It can be seen, that the iron loss is highly dependent on the injection orientation, corresponding to the different levels of flux linkage distortion as previously highlighted in Fig. 9. As a result, the d-axis CHI induces the highest iron loss, while the q-axis and the dq-axes (DFTC) CHIs show significantly lower iron loss, with the latter being the lowest as the flux linkage amplitude is directly controlled.

In order to sum up, the total loss due to CHIs at the rated speed along with the peak-to-peak torque ripple ΔT are depicted in Fig. 13. While the torque ripple can be properly compensated by means of the different CHIs, the dq-axes CHI based on DFTC provides an optimal solution in terms of total loss minimization in the full torque operation range of the considered IPMSM.

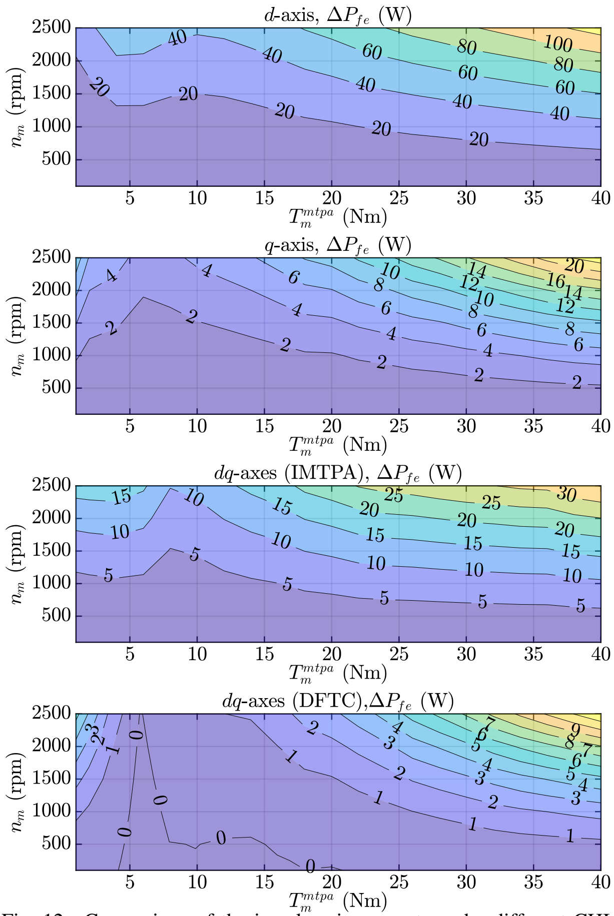

Fig. 12. Comparison of the iron loss increments under different CHIs.

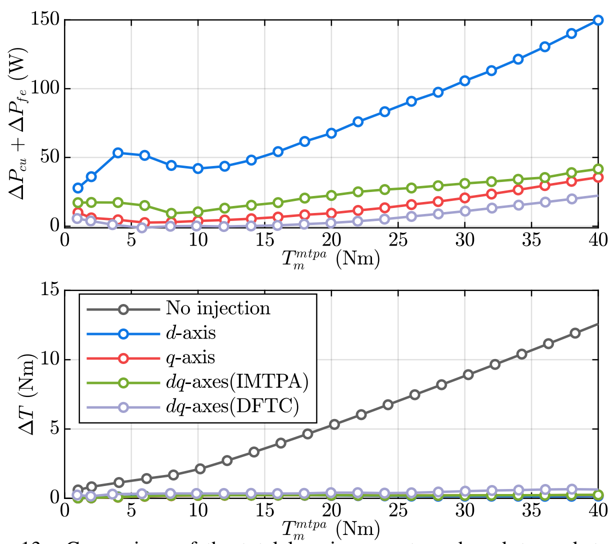

Fig. 13. Comparison of the total loss increments and peak-to-peak torque ripple under different CHIs at the rated speed.

Conclusion

This paper has presented a comprehensive analysis of torque ripple compensation for IPMSM considering the minimum loss under different CHIs. It has been shown by means of FE simulations that the torque ripple can be compensated by the d-axis, q-axis, and dq-axes (IMTPA and DFTC) CHIs, incurring different levels of flux linkage distortion and associated losses. Even though the dq-axes CHI based on IMTPA provides the minimum copper loss, the induced iron loss might compromise the total loss minimization. The dq-axes CHI based on DFTC generates a slightly higher copper loss, while the iron loss is significantly lower as the flux linkage is directly controlled, thus resulting in an optimal solution for the considered IPMSM.

Acknowledgment

This work has been supported by the COMET-K2 "Center for Symbiotic Mechatronic" of the Linz Center of Mechatronics (LCM) funded by the Austrian federal government and the federal state of Upper Austria, and in part by the Power Electronics Innovation Center (PEIC) of Politecnico di Torino.

Appendix

The main data of the considered prototype are provided in Table I.

TABLE I
Ratings of the Considered Motor

Parameter	Value
Number of pole pairs/slots	2/36
Nominal DC-link voltage	310 V
Nominal/maximum current	22/44 Apk
Nominal/maximum torque	18/43 Nm
Nominal/maximum speed	2500/9000 rpm

References

[1] G. Pellegrino, A. Vagati, P. Guglielmi, and B. Boazzo, "Performance comparison between surface-mounted and interior pm motor drives for electric vehicle application," *IEEE Trans. Ind. Electron.*, vol. 59, no. 2, pp. 803–811, 2012.

[2] G. Berardi, M. Bonfante, and N. Bianchi, "Analysis guideline to determine capabilities of ipm motors for automotive application," in *Proc. IEEE Int. Electric Mach. Drives Conf.*, 2019, pp. 957–964.

[3] N. Bianchi, M. Degano, and E. Fornasiero, "Sensitivity analysis of torque ripple reduction of synchronous reluctance and interior pm motors," *IEEE Trans. Ind. Appl.*, vol. 51, no. 1, pp. 187–195, 2015.

[4] M. S. Rafaq, W. Midgley, and T. Steffen, "A review of the state of the art of torque ripple minimization techniques for permanent magnet synchronous motors," *IEEE Trans. Ind. Informat.*, vol. 20, no. 1, pp. 1019–1031, 2024.

[5] A. Bojoi, P. Pescetto, F. Stella, S. Ferrari, and G. Pellegrino, "Direct flux-and-torque vector control with active torque ripple minimization," in *Proc. IEEE Appl. Power Electron. Conf. Expo.*, 2024, pp. 1028–1034.

[6] S. Ferrari, G. Pellegrino, M. Davoli, and C. Bianchini, "Reduction of torque ripple in synchronous reluctance machines through flux barrier shift," in *Proc. 23rd Int. Conf. Elect. Mach*, 2018, pp. 2290–2296.

[7] M. Xu, W. Zhao, J. Ji, Q. Chen, and G. Liu, "Auxiliary notching rotor design to minimize torque ripple for interior permanent magnet machines," *IEEE Trans. Ind. Electron.*, pp. 1–12, 2024.

[8] V. Varvolik, G. Buticchi, D. Prystupa, S. Wang, A. Aboelhassan, S. Peresada, and M. Galea, "Comparative study on torque ripple reduction considering minimum losses for synchronous reluctance motor drives," *IEEE Trans. Transport. Electrific.*, pp. 1–1, 2023.

[9] W. Qian, S. Panda, and J.-X. Xu, "Torque ripple minimization in pm synchronous motors using iterative learning control," *IEEE Trans. Power Electron.*, vol. 19, no. 2, pp. 272–279, 2004.

[10] G. Feng, C. Lai, J. Tian, and N. C. Kar, "Multiple reference frame based torque ripple minimization for pmsm drive under both steady-state and transient conditions," *IEEE Trans. Power Electron.*, vol. 34, no. 7, pp. 6685–6696, 2019.

[11] M. Tang, A. Formentini, S. A. Odhano, and P. Zanchetta, "Torque ripple reduction of pmsms using a novel angle-based repetitive observer," *IEEE Trans. Ind. Electron.*, vol. 67, no. 4, pp. 2689–2699, 2020.

[12] J. Qu, P. Zhang, J. Jatskevich, and C. Zhang, "Torque ripple reduction of permanent magnet synchronous machine drives based on novel speed harmonic control at low-speed operation," *IEEE Trans. Ind. Electron.*, pp. 1–11, 2022.

[13] P. B. Beccue and S. D. Pekarek, "A coupled piezoelectric/single-hall-sensor position observer for permanent magnet synchronous machines," *IEEE Trans. Ind. Electron.*, vol. 54, no. 5, pp. 2389–2397, 2007.

[14] J. Qu, J. Jatskevich, C. Zhang, and S. Zhang, "Torque ripple reduction method for permanent magnet synchronous machine drives with novel harmonic current control," *IEEE Trans. Energy Convers.*, vol. 36, no. 3, pp. 2502–2513, 2021.

[15] N. Nakao and K. Akatsu, "Suppressing pulsating torques: Torque ripple control for synchronous motors," *IEEE Ind. Appl. Mag.*, vol. 20, no. 6, pp. 33–44, 2014.

[16] K. Yamazaki, K. Utsunomiya, and H. Ohiwa, "Mechanism of torque ripple generation by time and space harmonic magnetic fields in permanent magnet synchronous motors," *IEEE Trans. Ind. Electron.*, vol. 69, no. 10, pp. 9884–9894, 2022.

[17] P. Chapman, S. Sudhoff, and C. Whitcomb, "Optimal current control strategies for surface-mounted permanent-magnet synchronous machine drives," *IEEE Trans. Energy Convers.*, vol. 14, no. 4, pp. 1043–1050, 1999.

[18] Z. S. Peng Yi, Xinjian Wang, "Interior permanent magnet synchronous motor minimum current harmonics torque ripple suppression strategy based on magnetic co-energy model," *IET Elect. Power Appl.*, vol. 14, pp. 234–244(10), February 2020.

[19] C. Lai, G. Feng, K. Mukherjee, V. Loukanov, and N. C. Kar, "Torque ripple modeling and minimization for interior pmsm considering magnetic saturation," *IEEE Trans. Power Electron.*, vol. 33, no. 3, pp. 2417–2429, 2018.

[20] D. Flieller, N. K. Nguyen, P. Wira, G. Sturtzer, D. O. Abdeslam, and J. Mercklé, "A self-learning solution for torque ripple reduction for nonsinusoidal permanent-magnet motor drives based on artificial neural networks," *IEEE Trans. Ind. Electron.*, vol. 61, no. 2, pp. 655–666, 2014.

[21] B. A. Basit, H. H. Choi, and J.-W. Jung, "An online torque ripple minimization technique for ipmsm drives: Fuzzy system-based d-axis current design approach," *IEEE Trans. Ind. Electron.*, vol. 68, no. 12, pp. 11 794–11 805, 2021.

[22] J. Qu, P. Zhang, and J. Jatskevich, "Harmonic current optimization for torque ripple reduction in permanent magnet synchronous machine drives based on torque ripple surrogate model," *IEEE Trans. Power Electron.*, pp. 1–11, 2024.

[23] H.-J. Cho, Y.-C. Kwon, and S.-K. Sul, "Torque ripple-minimizing control of ipmsm with optimized current trajectory," *IEEE Trans. Ind. Appl.*, vol. 57, no. 4, pp. 3852–3862, 2021.

[24] H. Zhang, M. Dou, and J. Deng, "Loss-minimization strategy of non-sinusoidal back emf pmsm in multiple synchronous reference frames," *IEEE Trans. Power Electron.*, vol. 35, no. 8, pp. 8335–8346, 2020.

[25] J. Qu, P. Zhang, C. Zhang, and S. Zhang, "Torque ripple reduction method for interior permanent magnet synchronous machine drives with minimal loss," in *IEEE Energy Convers. Congr. Expo.*, 2022, pp. 1–7.

[26] H. Zhang, M. Dou, and C. Dang, "Loss-optimization method of permanent-magnet synchronous motor based on precise stator iron loss model," *IEEE Trans. Emerg. Sel. Topics Power Electron.*, vol. 9, no. 5, pp. 5407–5415, 2021.

[27] A. Ruf, S. Steentjes, A. Thul, and K. Hameyer, "Stator current vector determination under consideration of local iron loss distribution for partial load operation of pmsm," *IEEE Trans. Ind. Appl.*, vol. 52, no. 4, pp. 3005–3012, 2016.

[28] N. Bianchi, S. Bolognani, D. Bon, and M. Dai PrÉ, "Torque harmonic compensation in a synchronous reluctance motor," *IEEE Trans. Energy Convers.*, vol. 23, no. 2, pp. 466–473, 2008.

[29] M. Barcaro, N. Bianchi, and F. Magnussen, "Remarks on torque estimation accuracy in fractional-slot permanent-magnet motors," *IEEE Trans. Ind. Electron.*, vol. 59, no. 6, pp. 2565–2572, 2012.

[30] V. Varvolik, G. Buticchi, S. Wang, D. Prystupa, S. Peresada, S. Bozhko, and M. Galea, "High-fidelity model identification for synchronous reluctance motor drives," *IEEE Trans. Energy Convers.*, vol. 38, no. 4, pp. 2623–2633, 2023.

[31] A. Varatharajan, P. Pescetto, S. Ferrari, and G. Pellegrino, "Flux maps spatial harmonic modeling and measurement in synchronous reluctance motors," in *IEEE Energy Convers. Congr. Expo*, 2023, pp. 4868–4873.

[32] Z.-Q. Zhu, S. Xue, W. Chu, J. Feng, S. Guo, Z. Chen, and J. Peng, "Evaluation of iron loss models in electrical machines," *IEEE Trans. Ind. Appl.*, vol. 55, no. 2, pp. 1461–1472, 2019.

[33] S.-H. Han, T. M. Jahns, and Z. Q. Zhu, "Analysis of rotor core eddy-current losses in interior permanent magnet synchronous machines," in *2008 IEEE Ind. Appl. Soc. Annu. Meeting.*, 2008, pp. 1–8.

[34] S.-C. Yang and R. D. Lorenz, "Analysis of iron and magnet losses in surface-permanent-magnet machines resulting from injection-based self-sensing position estimation," *IEEE Trans. Ind. Appl.*, vol. 48, no. 6, pp. 1901–1910, 2012.

Vasyl Varvolik received the M.Sc. degree in Electrical Engineering from the National Technical University of Ukraine "Igor Sikorsky Kyiv Polytechnic Institute", Kyiv, Ukraine in 2018, and a Ph.D. degree from the University of Nottingham, Ningbo, China in 2024. He is currently a Postdoctoral Researcher with the Institute of Electrical Drives and Power Electronics, Johannes Kepler University, Linz, Austria.

Paolo Pescetto received the M.Sc. and Ph.D. degrees in Electrical Engineeri from Politecnico di Torino, Turin, Italy, in 2015 and 2019, respectively. Since 2019, he has been a Researcher and tenure-track Lecturer with the Energy Department, Politecnico di Torino. He is a Member of the Power Electronics Innovation Center (PEIC), Politecnico di Torino.

Simone Ferrari received the Ph.D. degree "cum laude" in 2020 from Politecnico di Torino, Turin, Italy, where he is currently a Research Fellow. From July to December 2018, he was a Visiting Scholar with North Carolina State University, Raleigh, NC, USA. He is a Member of the Power Electronics Innovation Center (PEIC), Politecnico di Torino.

Shuo Wang received the Ph.D. degree in control science and engineering from Tongji University in 2019, Shanghai, China. From 2017 to 2018, he became a Visiting researcher with Power Electronics, Machines and Control Group (PEMC Group), University of Nottingham, Nottingham, U.K. He is currently working as a senior research fellow at the University of Nottingham, Ningbo, China.

Michele Degano received the M.Sc degree in Electrical Engineering from the University of Trieste, Italy, in 2011, and his Ph.D. degree in Industrial Engineering from the University of Padova, Italy, in 2015. He is currently the PEMC Director of Industrial Liaison leading research projects for the development of hybrid electric aerospace platforms and electric transports.

Giampaolo Buticchi received the M.Sc. degree in Electronic Engineering in 2009 and the Ph.D. degree in Information Technologies in 2013 from the University of Parma, Italy. In 2012, he was a visiting researcher at the University of Nottingham, UK. Between 2014 and 2017, he was a post-doctoral researcher at the University of Kiel, Germany. He is now Professor of Electrical Engineering at the University of Nottingham, Ningbo, China.

Gianmario Pellegrino received the M.Sc. and Ph.D. degrees in electrical engineering from Politecnico di Torino, Turin, Italy, in 1998 and 2002, respectively. He is currently a Professor of power converters, electrical machines and drives with Politecnico di Torino. He was a Visiting Fellow with Aalborg University, Denmark, the University of Nottingham, U.K., and the University of Wisconsin, Madison, USA. He is one of the authors of the open, source project SyRe for the design of electrical motors and three patents. He is engaged in several research projects with the industry. Dr. Pellegrino is an Associate Editor for the IEEE Transactions on Industry Applications. He was the recipient of more than 55 IEEE journal papers and nine Best Paper Awards. He is a member of the Power Electronics Interdepartmental Laboratory (PEIC) established in 2017 at the Politecnico di Torino and a member of the Advisory Board of PCIM (Power Conversion and Intelligent Motion) Europe. He is currently the Rector's Advisor for Interdepartmental Centres, Politecnico di Torino.